MICROROBOTS

Control of molecular shuttles by designing electrical and mechanical properties of microtubules

Naoto Isozaki,[1] Hirofumi Shintaku,[1] Hidetoshi Kotera,[1] Taviare L. Hawkins,[2] Jennifer L. Ross,[3] Ryuji Yokokawa[1]*

Kinesin-driven microtubules have been focused on to serve as molecular transporters, called "molecular shuttles," to replace micro/nanoscale molecular manipulations necessitated in micro total analysis systems. Although transport, concentration, and detection of target molecules have been demonstrated, controllability of the transport directions is still a major challenge. Toward broad applications of molecular shuttles by defining multiple moving directions for selective molecular transport, we integrated a bottom-up molecular design of microtubules and a top-down design of a microfluidic device. The surface charge density and stiffness of microtubules were controlled, allowing us to create three different types of microtubules, each with different gliding directions corresponding to their electrical and mechanical properties. The measured curvature of the gliding microtubules enabled us to optimize the size and design of the device for molecular sorting in a top-down approach. The integrated bottom-up and top-down design achieved separation of stiff microtubules from negatively charged, soft microtubules under an electric field. Our method guides multiple microtubules by integrating molecular control and microfluidic device design; it is not only limited to molecular sorters but is also applicable to various molecular shuttles with the high controllability in their movement directions.

INTRODUCTION

Kinesin motor proteins and microtubule (MT) cytoskeletal filaments show promise as an in vitro nanoscale actuator platform for nanobiotechnology applications. MTs are rigid, polar, dynamic cytoskeletal filaments that serve as mechanically supportive cellular structures. MTs also serve as the highway system for intracellular transport by kinesin and dynein motor proteins. This motor-driven active transport uses the hydrolysis of adenosine triphosphate (ATP) and is indispensable in terms of maintaining cellular functions (*1*, *2*). In the cell, kinesin motor proteins walk along MTs to deliver vesicular and small-molecule cargos to destinations in an in vivo viscous environment. The MT-kinesin transport system can be reconstituted in vitro for cargo transport or inverted to have molecular motors transport MTs.

The MT-kinesin system can be combined with microfluidics for enabling simultaneous control of aqueous, bulk chemical composition with the direct transport of molecular-scale cargos. These systems promise an unprecedented control over nanoscale delivery—not just bulk flow and chemical reactions—and have matured into micro total analysis systems (μTAS) that could replace on-chip functions (*3*–*5*). These μTAS enable a wide range of applications using motor-driven MTs as molecular shuttles, such as molecular transporters, sorters, concentrators, and detectors. MT-kinesin μTAS load cargos onto gliding MTs via avidin-biotin binding (*5*, *6*), antigen-antibody interaction (*7*, *8*), or DNA hybridization (*9*, *10*) to be sorted, transported, and detected on a chip. Although individual functions have been demonstrated, a long-lasting challenge that hampers practical usage of MT-kinesin is the directional control of gliding MT shuttles, because they glide in random directions due to Brownian motion acting on the free leading tip (minus ends). MT trajectories can be controlled by photoresist tracks (*5*, *11*, *12*), fluid shear flow (*13*, *14*), magnetic fields (*15*), and electric fields (*16*–*18*). However, these methods limit the control of MT transport to only one destination; without an active control, all MT shuttles behave in the same manner and glide toward the same destination (*16*). We tackled this challenge of multiple-cargo sorting by integrating a bottom-up molecular design of MTs and a top-down design of the microfluidic device. Using these methods, we demonstrate MT gliding to two destinations as a highly efficient MT sorter under a single external field.

For the bottom-up manipulation of MTs, we focused on two MT properties to be exploited: electrical and mechanical properties. Our group has already reported that the surface charge density of MTs is negatively correlated with the radius of the trajectory curvature (*19*). The design of the MT surface charge density enabled us to guide MTs toward multiple directions under a given electric field. Here, we additionally manipulate the mechanical stiffness of the MTs measured as flexural rigidity (κ) or persistence length (L_p). In vivo, MTs control their stiffness depending on the intracellular roles of the filament; that is, stiffer MTs are needed in the axon to support its long structure, whereas more flexible MTs are needed in a proliferating cell to enable rapid redistribution (*20*). Many factors altering MT stiffness have been reported, including MT stabilizing agents, nucleotides, MT-associated proteins (MAPs), and growth rates. However, there are still controversies on stiffening and softening factors, and the measured stiffness has not been used to manipulate MT gliding directions (*17*, *20*–*38*). The cantilever beam model suggests that MT stiffness is proportional to the persistence of the gliding trajectory (*19*), so we proposed to design both the electrical and the mechanical properties simultaneously to improve controllability of the gliding directions. We predicted that MTs with low surface charge density and high stiffness will have larger radii of curvature trajectories (longer persistence) than those with high surface charge density and low stiffness (Fig. 1).

We first investigated the stiffness of MTs to find the maximum and minimum rigidity under various polymerizing conditions—using nucleotides, growth rate, and the neuronal MAP, tau (*25*). The L_p of the designed MTs was measured using thermal fluctuations, and the relationship of L_p to the gliding trajectories under an electric field was obtained. We further modified the electrical properties of MTs by

[1]Department of Micro Engineering, Kyoto University, Kyoto-Daigaku Katsura, Nishikyo-ku, Kyoto 615-8540, Japan. [2]Department of Physics, University of Wisconsin–La Crosse, 1725 State Street, La Crosse, WI 54601, USA. [3]Department of Physics, University of Massachusetts Amherst, 666 North Pleasant Street, Amherst, MA 01003, USA.
*Corresponding author. Email: ryuji@me.kyoto-u.ac.jp

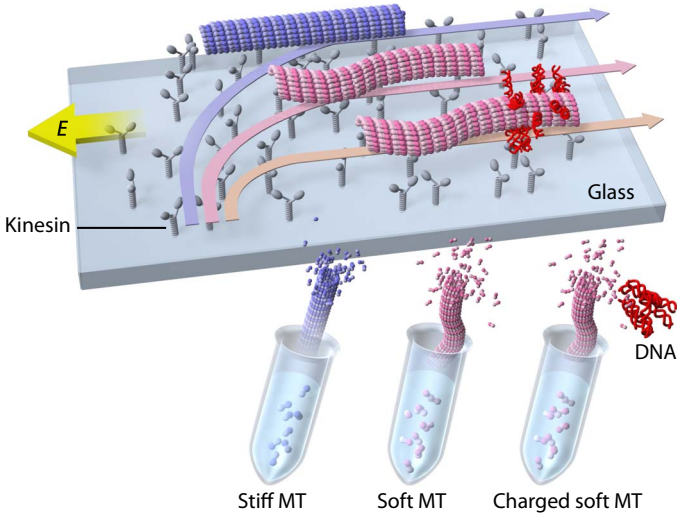

Fig. 1. Schematic representation of MT sorting under a given electric field. Designing MT properties controls the trajectories of kinesin-propelled MTs. Various types of MTs were polymerized under different conditions in microtubes. When an electric field, *E*, is applied perpendicular to gliding MTs, their gliding directions are gradually oriented toward the anode. MTs are transported toward different destinations corresponding to their stiffness and surface charge density.

labeling filaments with DNA. We have shown that the addition of DNA to MTs can alter the radius of curvature by 2.3-fold (*19*). In addition to the bottom-up designs of the MT electrical and mechanical properties, we took a top-down approach to design a microfluidic device that separates MTs according to measured radii of trajectory curvatures (Fig. 1). This integrated approach enabled us to guide two types of MTs toward two different destinations and separate them in the device corresponding to their properties, resulting in MT sorting at about 80% efficiency.

Our work establishes a bottom-up methodology for directional control of molecular shuttles and a top-down methodology for optimal design of microfluidic devices. Using this strategy, molecular shuttles can transport toward separate designated destinations to realize a goal of autonomous, on-chip, differential sorting of molecular shuttles as demonstrated here. This step is instrumental for enabling on-chip sorting of cargos without outside intervention for each shuttle and would open the door to further autonomous actions that require sorting, such as sensing and response.

RESULTS

Variable persistence length under different polymerizing conditions

We investigated five types of MTs listed in Table 1: tau-bound slowly polymerized guanylyl(α,β)methylenediphosphonate (GMPCPP)–MT (MT-1), tau-free slowly polymerized GMPCPP-MT (MT-2), tau-bound slowly polymerized guanosine triphosphate (GTP)–MT (MT-3), tau-free slowly polymerized GTP-MT (MT-4), and tau-free quickly polymerized GTP-MT (MT-5). Each MT type was elongated as segments from short MT seeds made in the presence of GMPCPP. The GMPCPP tubulin dimers were biotinylated to immobilize them onto a glass substrate to ultimately measure their L_p. The growth rate in the elongation process was controlled by using either 10 or 30 μM free tubulin polymerized in the presence of GTP (Fig. 2A). To measure the length of the elongated segments, we sampled MTs 0.5 to 60 min after elongation started, and all MTs were stabilized by paclitaxel just after sampling.

Table 1. The five MTs investigated.

Name	MT-1	MT-2	MT-3	MT-4	MT-5
Growth rate	Slow				Fast
Nucleotide	GMPCPP		GTP		
Tau binding	Yes	No	Yes	No	

To determine the lengths of the elongated segments with respect to time, we plotted the distribution of MT length and fit it to Gaussian functions to find the mean and SD (fig. S1). Only the normally distributed data were used and plotted (Fig. 2A). As expected, MTs elongated linearly in the first several minutes and then reached plateaus. Data were fitted as solid lines by an exponential decay, $L(t) = L_{max}[1 - \exp(-t/\tau)]$, where L is the MT length over time, t, L_{max} is the upper limit of L, and τ is the characteristic time constant. τ and L_{max} were 1.53 min and 6.22 μm for 30 μM tubulin (R^2 = 0.94) and 10.8 min and 4.28 μm for 10 μM tubulin (R^2 = 0.94), respectively. Growth rates defined by the slopes at early times (dashed lines) were calculated as 2.19 ± 0.15 μm min^{-1} for 30 μM tubulin (R^2 = 0.92) and 0.303 ± 0.017 μm min^{-1} for 10 μM tubulin (R^2 = 0.93). These two concentrations successfully controlled the growth rate, and MTs elongated faster at higher tubulin concentrations, as expected. The measured growth rates are within the range of previous in vitro experiments (0.135 to 2.56 μm min^{-1}) (*39*–*45*).

The L_p was measured for MT-1 to MT-5 (Fig. 2, B to G). The biotinylated seed was immobilized onto a glass substrate via biotin-streptavidin, and the elongated segment was free to fluctuate under Brownian motion (Fig. 2, B and C, and movie S1). Fluorescent images of MTs were converted to binary images and skeletonized via Gaussian fitting using the MT tracking software, fluorescence image evaluation software for tracking and analysis (FIESTA) (Fig. 2, C to F) (*46*). L_p was derived by equating thermal energy with bending energy of MTs, on the assumption that a freely fluctuating segment behaved as a cantilever beam clamped at the immobilized biotinylated segment (see the Supplementary Materials and fig. S2 for details). For each type of MT, the distribution of L_p was measured and shown to have a normal distribution (fig. S3). MTs were categorized into three groups according to L_p (Fig. 2G): stiff MTs (MT-1 and MT-2), soft MT (MT-5), and intermediate MTs (MT-3 and MT-4). From our data, we see no significant differences between MT-1 and MT-2, or MT-3 and MT-4, implying that the tau binding did not affect L_p of either GTP- or GMPCPP-polymerized MTs when MTs were slowly polymerized. The nucleotide had a substantial effect on the L_p, because significant differences were found between MT-1 and MT-3 and between MT-2 and MT-4. From our work, we observe that L_p increased about two-fold when GTP was replaced by GMPCPP at 10 μM tubulin. Last, the dependence of L_p on the growth rate was significant, as demonstrated by the difference between MT-4 and MT-5: L_p decreased about 2.5-fold with the increase of growth rate from 0.303 to 2.19 μm min^{-1}. Therefore, we obtained three MT groups with different L_p values by changing the nucleotide and growth rate during polymerization. In addition, the length of the fluctuating segments ranged from 2 to 17 μm, and

we found no correlation between the filament contour length and L_p (fig. S4).

Dependence of radius of trajectory curvature on MT properties

When an electric field is applied in the negative x direction of the xy plane and the MTs enter the field at the origin in the positive y direction, the MT trajectory is defined as follows:

$$y(x) = R_{MT} \cdot \arccos\left(e^{-\frac{x}{R_{MT}}}\right) \quad (1)$$

$$R_{MT} = \frac{3k_B T L_p}{c_\perp(\mu_{el} - \mu_{EOF})E\langle d\rangle^2} \quad (2)$$

where k_B is the Boltzmann constant, T is the temperature, $c_\perp$ is the perpendicular Stokes drag coefficient per unit length of an MT tethered to the surface via kinesin, μ_{el} is electrophoretic mobility, μ_{EOF} is electroosmotic mobility, E is the electric field intensity, and $\langle d\rangle$ is the average deformed length of the MT leading tips due to the electrical force (*16*, *17*). The electric field biases the MT gliding directions toward the anode with the curvature parameter, R_{MT}, corresponding to the radius of the curvature. MT-1 and MT-2 had the maximum L_p, and MT-5 had the minimum, as shown in Fig. 2G. This allowed us to select MT-1 and MT-2 for large R_{MT} and MT-5 for small R_{MT}. To further decrease R_{MT} by increasing the μ_{el} of MTs, we selected MT-5 for labeling with 50–base pair (bp) DNA (*19*). Thus, three MT groups with different R_{MT} were prepared: MT-1 or MT-2 (stiff MT, large R_{MT}), MT-5 (soft MT, middle R_{MT}), and DNA-labeled MT-5 (negatively charged soft MT, small R_{MT}). Types MT-1, MT-2, and MT-5 were polymerized under the designated conditions, as shown in Table 1. For the shuttle-gliding experiments, MTs did not have seed segments in contrast to MTs prepared for measuring the growth rate and L_p. DNA-labeled MT-5 consisted of a short biotinylated MT-5 segment at the minus end and an elongated nonlabeled MT-5 segment at the plus end. This design was used to prevent the steric hindrance that disturbs the MT gliding if the entire MT surface is coated with streptavidin and DNA molecules (*47*). Moreover, it was sufficient to label only the short minus-end segment with DNA because the gliding direction depends on the properties of the MT leading tips with the length of $\langle d\rangle$. Hereafter, the partially DNA-labeled MT is referred to as MT-5′.

These four MT types were assayed in a microfluidic channel to directly measure the R_{MT} under an electric field (Fig. 3A). The channel was fabricated with polydimethylsiloxane (PDMS) to have a 10-μm height. After nonspecific adsorption of α-casein and kinesin to the PDMS channel, MT gliding was initiated by 0.5-mM ATP. An applied electric field of 5.3 kV m^{-1} guided the MTs toward the anode, and R_{MT}—as defined by Eq. 1—was measured (Fig. 3B).

We measured the normalized R_{MT} values for the four MT types (Fig. 3C), which could be categorized into three groups: MTs with large (a, MT-1 and MT-2), middle (b, MT-5), and small (c, MT-5′) R_{MT} (fig. S5 shows the raw data). We found no correlation between MT contour length and R_{MT} (fig. S6). The insignificant difference between MT-1 and MT-2, and the significant difference between (i) MT-1 and MT-2 and (ii) MT-5 reflect the differences in the L_p values as shown in Fig. 2G. This positive correlation between R_{MT} and L_p follows Eq. 2. In addition, MT-5′ showed significantly smaller R_{MT} than MT-5. The increase of μ_{el} of the leading tips via DNA labeling decreased the R_{MT}, which also followed Eq. 2. Therefore, R_{MT} was controlled by designing L_p and μ_{el}; larger L_p and smaller μ_{el} produced large R_{MT}. To test the sorting, we used either MT-2 and MT-5 or MT-2 and MT-5′.

Device design and MT sorting

The microfluidic device was designed on the basis of the measured R_{MT} values: 40.3 μm (n = 90) for MT-2, 21.0 μm (n = 57) for MT-5, and 14.5 μm (n = 39) for MT-5′, all under 5.3 kV m^{-1}. We considered three points for defining the dimensions of the device: (i) The separation channel needs to have a width of <1 mm to obtain a uniform electric field (*48*); (ii) the cross-contamination should be decreased by increasing the difference of R_{MT} to be used as a molecular sorter; (iii) to observe the MT separation in the field of view, the travel distance in the y direction of either MT group should be less than 80 μm. Because Eq. 2 suggests that the difference in R_{MT} is inversely proportional to the field intensity, we recalculated R_{MT} with a field intensity of 3 kV m^{-1}, and the MT trajectories were predicted with Eq. 1; traveling distances in the y direction were 84.6 μm for MT-2, 58.8 μm for MT-5, and 35.2 μm for MT-5′ at x = 70 μm (fig. S7). Therefore, we set the separation wall at (x, y) = (≥70 μm, 70 μm) to demonstrate the separation of MT-2 from MT-5 and MT-2 from MT-5′ using the same device.

The device can be divided into three areas: MT landing area, MT alignment area, and MT sorting area with the MT separation wall (Fig. 4, A to C). MTs landed only on the landing area surface due to the flow generated by pressure differences between reservoirs C and D. The filament gliding directions were aligned to the y axis in the alignment area after ATP was introduced. An electric field subsequently rectified the direction of the MTs toward the anode with a different R_{MT} reflecting their L_p and μ_{el} in the sorting area.

Figure 4D shows the sequential images for MT immobilization in the landing area. The number of landing MTs increased with time, and no MT was observed in any other areas. MT alignment was evaluated by comparing the SD of the MT orientation angles in the landing area (Fig. 4, E and G) and in the alignment area (Fig. 4, F and H). The orientation angle was defined as the angle between the x axis and the measured MT gliding direction. Orientation angles in the alignment area (0.49 ± 0.04 rad, n = 35, mean ± SD) showed a significantly smaller SD than those in the landing area (0.44 ± 0.27 rad, n = 70). Therefore, the MT gliding directions were oriented toward the positive y axis direction in the alignment area.

We tracked trajectories in the sorting area for MT-2 and MT-5 (Fig. 4I and movie S2) or MT-2 and MT-5′ (Fig. 4J and movie S3). The sorting efficiency was evaluated by counting the number of MTs separated by the wall. When MT-2 and MT-5 were tested together (n = 129), 84.4% of MT-2 glided above and 57.7% of MT-5 glided below the wall. When MT-2 and MT-5′ were tested together (n = 159 in four experiments), 80.4% of MT-2 and 90.4% of MT-5′ were guided above and below the wall, respectively. By comparing these results, we demonstrated two significant advances in autonomous MT sorting: The sorting efficiency reached about 60% by designing L_p of MT under different polymerizing conditions, and the efficiency was significantly improved to about 80% by the additive effects of μ_{el} to L_p.

DISCUSSION

To create a device that sorts MT shuttles, we modified the electrical and mechanical properties of MTs. The mechanical characteristic, L_p, was carefully investigated by changing growth rates, nucleotide types, and the presence of tau protein. First, we tested the growth rate using two

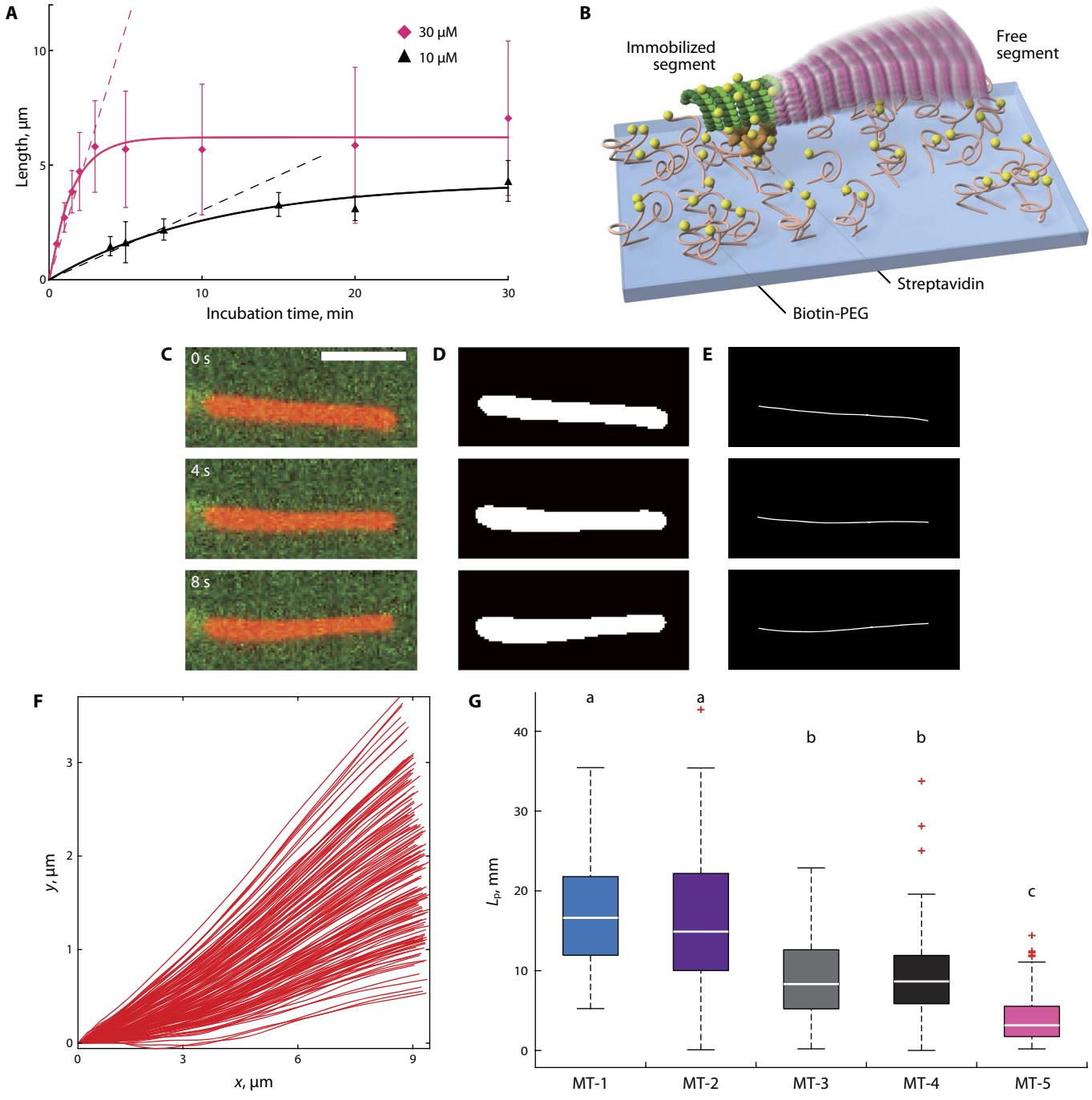

Fig. 2. Control of MT persistence length by polymerizing conditions. (**A**) Time course of MT length in the presence of 30 μM (red diamonds) and 10 μM tubulin concentrations (black triangles). Means ± SD are shown. Solid lines show the best fit to an exponential function using the least-squares method. Dashed lines show least-squares fitting of lines for the first several minutes ($R^2 > 0.92$). (**B**) The schematic representation of the measurement system. MTs were partially immobilized onto a biotin-coated substrate by streptavidin and biotinylated MT seeds. (**C**) Sequential images of a fluctuating MT (red). The left segment (light green) was immobilized. Scale bar, 5 μm. Images were (**D**) binarized and (**E**) skeletonized with the FIESTA software. (**F**) Superposition of the whole shape of a fluctuating MT for each frame. (**G**) Box plots of L_p for MT-1 ($n = 114$ measurements), MT-2 ($n = 128$), MT-3 ($n = 100$), MT-4 ($n = 86$), and MT-5 ($n = 126$). Red plus signs are outliers that are above the third quartiles by 1.5 interquartile ranges. There are no significant differences between identical lowercase letters by the Steel-Dwass test at a critical value of $P < 0.01$.

different tubulin concentrations (10 and 30 μM). The lengths of the MTs reached plateaus due to the noncovalent polymers being in dynamic equilibrium with the background concentration of free tubulin (Fig. 2A). As MTs polymerize, the number of free tubulin molecules decreases, and some MTs transition from polymerization to catastrophe, which releases tubulin from the filament. Thereafter, tubulin molecules are supplied by catastrophes, and individual MTs can grow and shrink. Although the periodic transition between catastrophes and rescues,

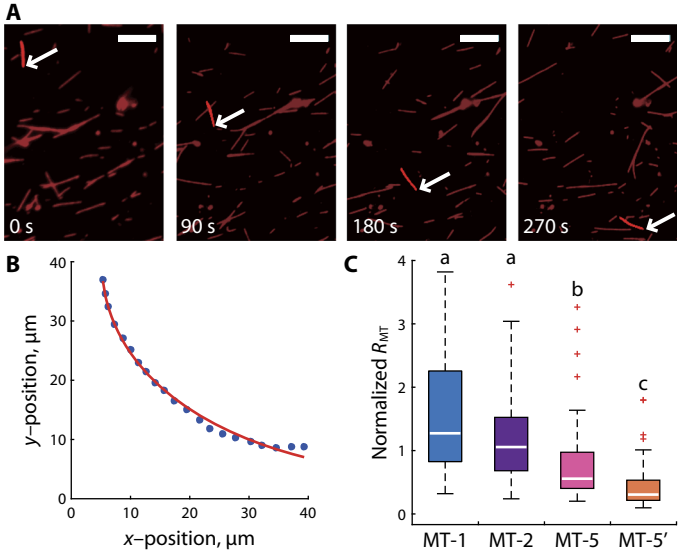

Fig. 3. Control of MT gliding directions via the bottom-up designing of MT electrical and mechanical properties. (**A**) Sequential images of a gliding MT-2 (highlighted). An electric field of 5.3 kV m^{-1} was applied from the right- to the left-hand side of images. White arrows indicate the leading tip of the MT. Scale bars, 10 μm. (**B**) Trajectory and fitted result for the MT shown in (A). The leading tip was tracked (blue dots) and fitted with Eq. 1 as a red line (R^2 = 0.99) to obtain R_{MT}. (**C**) Box plots of normalized R_{MT} for MT-1 (n = 32), MT-2 (n = 141), MT-5 (n = 62), and MT-5′ (n = 62). R_{MT} were normalized to mean R_{MT} for MT-2. Red plus signs are outliers that are above the third quartiles by 1.5 interquartile ranges. No significant differences were observed between MT-1 and MT-2 (a). MT-5 (b) and MT-5′ (c) showed significant differences with (a) and with each other, as determined by the Steel-Dwass test at a critical value of $P < 0.01$. MT trajectories followed Eq. 1 with $R^2 > 0.98$.

termed dynamic instability, increased the variation of MT length, the mean MT length becomes constant (*39*). The large SD of the MT length measurements (Fig. 2A) is due to the broad distribution of MT length in fig. S1 in the steady-state phase due to MT dynamic instability.

We found a significant difference in L_p resulting from different growth rates between MT-4 (slow) and MT-5 (fast) that agreed with previous reports, which suggested that higher growth rates produced softer MTs (*27*, *49*). L_p was measured as 3.2 mm for quickly polymerized MT-5, with a growth rate of 2.19 μm min^{-1} at a tubulin concentration of 30 μM. This result is consistent (within uncertainty) with the L_p ~ 3.4 mm reported previously for MTs polymerized at 2.40 μm min^{-1} under the tubulin concentration of 28 μM (*49*). L_p was 8.7 mm for the slowly polymerized MT-4 (growth rate of 0.303 μm min^{-1}). It is not surprising that such a low growth rate produced a higher L_p than 6.6 mm previously measured for the lowest reported growth rate (1.50 μm min^{-1}) (*27*). Recently, higher tubulin concentrations (that is, higher growth rates) were shown to induce more defects in the MT lattice structure, resulting in lower L_p (*50*). Our work verifies that faster growth rates result in more lattice defects, causing a lower measured L_p.

The difference in nucleotides between MT-2 (GMPCPP) and MT-4 (GTP) agrees with a common understanding: GMPCPP produces stiffer MTs than GTP due to the conformational change in the tubulin dimers, which is supported by previous experiments (*24*, *30*, *31*, *51*–*56*). However, we found that tau proteins did not show any effect on L_p in our study, which is different than previous studies. Hawkins *et al.* reported that copolymerizing tau at 1:100 (tau/tubulin) increased L_p (0.6 to 4 mm), and Felgner *et al.* reported that adding tau to polymerized MTs increased L_p with the increase of tau (0.92 to 2.5 mm) (*25*, *31*). This inconsistency is likely due to the growth rate differences between our work and previous work. The growth rate of each MT (MT-1 to MT-4) polymerized with and without tau was lower than previous works, which likely caused the higher L_p (8.3 to 17 mm). Thus, these MTs may be insensitive to the stiffening typically caused by the tau proteins due to their lack of defects. Previously, Hawkins *et al.* tested the effects of paclitaxel, tau, and nucleotide on the stiffness of MTs that were polymerized quickly and found that the order of the addition of various stabilizers affected the outcome (*31*). In the current case, we copolymerized with tau but very slowly. Thus, we conclude that the rate of polymerization, and likely the lack of filament defects, is a more effective regulator of MT stiffness (*23*, *57*).

The dependency of L_p on MT contour length is more controversial. Our results showed that L_p is independent of the contour length (fig. S4). Previous groups have measured L_p for MTs affixed at one end and cantilevered, as we measured here, and reported an increase of L_p with the increase of contour length (*26*, *30*, *58*). However, others have shown no dependency on a measured contour length for both affixed MTs (*25*, *27*, *59*) and freely fluctuating MTs (*31*, *34*, *35*, *53*, *60*, *61*). More recently, Zhang *et al.* argued that the dependency on length for affixed MTs is negligible for contour lengths of >2 μm by numerical simulation (*62*). This supports our results because we only used MTs longer than 2 μm for our L_p measurements. Our results contribute previously unknown understanding of the effects of growth rate on L_p. We could consistently measure and modulate L_p by the growth rate and nucleotide state to alter R_{MT} and enable MT sorting.

Our experimental setup for the measurement of L_p has two advantages. First, we affixed the biotinylated segment to the glass substrate, whereas the other, nonlabeled segment fluctuated in the solution, thus preventing MT rotation around the longitudinal axis. This rotation could conflate thermally activated bending with the rotation of a bent filament (*27*, *34*). Second, by using different fluorophores to label these segments, we could define the affixed segment in the image analysis, which enabled us to precisely find the clamped end of a fluctuating MT, as proposed in a previous study (*27*).

Assuming that the error introduced from locating the clamped end during the image analysis was minimized, larger errors stem from the MT fluctuating perpendicular (z direction) to the surface (xy plane) due to the height of the flow cell (10 μm). We observed the projection of MTs onto the xy plane and could underestimate MT deflection, leading to an overestimation of L_p. Fluctuations in the z direction add an uncertainty to L_p of up to 8% for the following reasons: The depth of field was 400 nm in our observation system, which means that the largest deflection detectable in the z direction was ~400 nm. Because MT deflection in the xy plane was 1 to 3 μm when the MT tip was elevated 400 nm from the xy plane, the actual deflection is from 1.08 μm ($\sqrt{1^2 + 0.4^2} \cong 1.08$) to 3.02 μm ($\sqrt{3^2 + 0.4^2} \cong 3.02$). Therefore, the maximum uncertainty of deflection is 8%, and the overestimation of L_p is less than 8%.

We have previously measured the electric characteristic parameters of MTs as follows: $c_\perp = 1.39 \times 10^{-2}$ kg m^{-1} s^{-1}, $\mu_{EOF} = 1.33 \times 10^{-8}$ m^2 V^{-1} s^{-1}, $\mu_{el} = 2.03 \times 10^{-8}$ m^2 V^{-1} s^{-1} for Alexa Fluor 488–labeled MTs, 2.09×10^{-8} m^2 V^{-1} s^{-1} for rhodamine-labeled MTs, and 3.02×10^{-8} m^2 V^{-1} s^{-1} for 50-bp DNA- and rhodamine-labeled MTs (*19*). By substituting these values and the measured R_{MT} into Eq. 2, we calculated the length of the deformed leading tips, $\langle d \rangle$, as 3.0 μm for MT-2, 1.8 μm for MT-5, and 1.5 μm for MT-5′. When all kinesin molecules attach to MTs without stretching, $\langle d \rangle$ values are theoretically

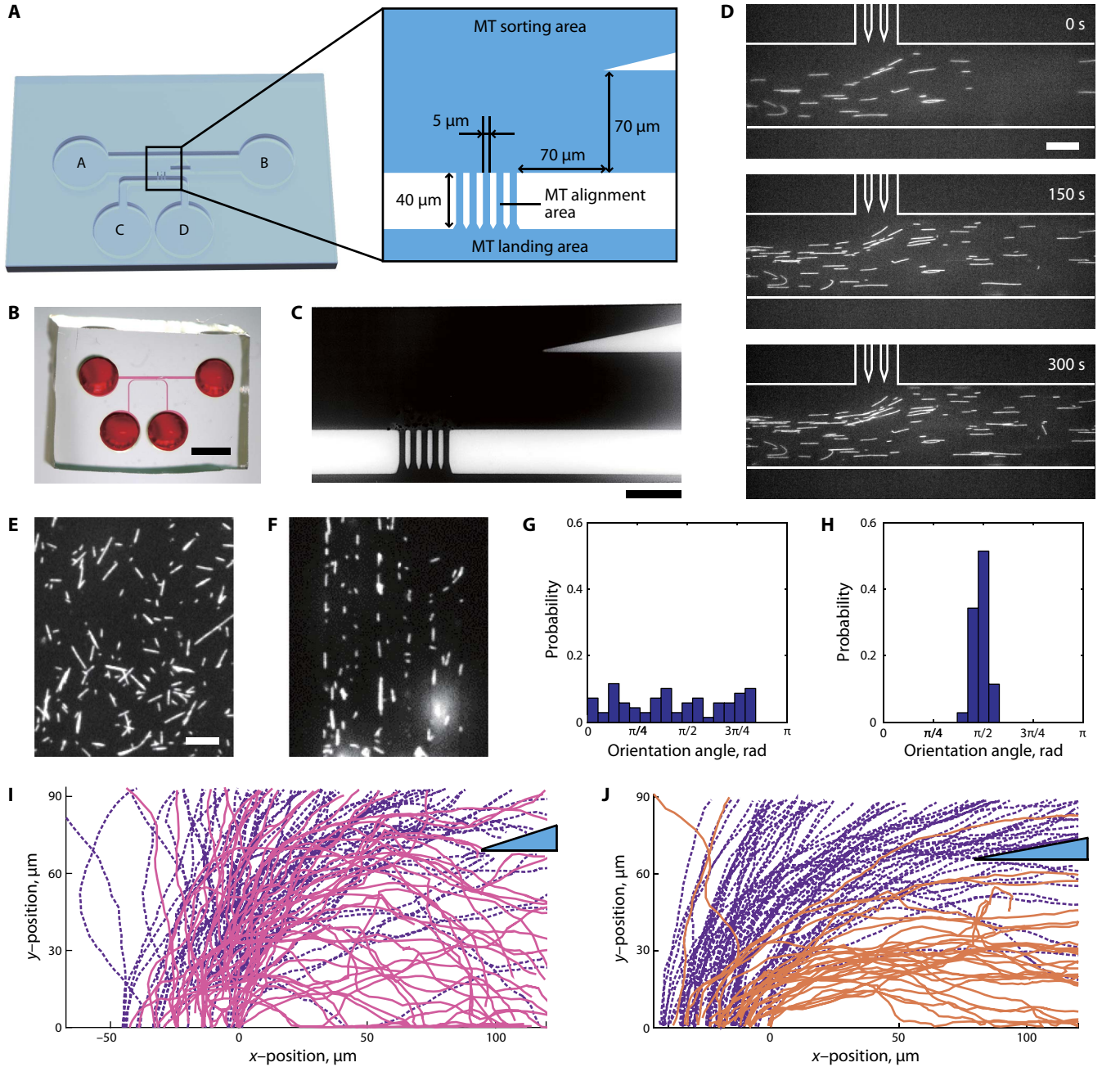

Fig. 4. Demonstration of MT sorting by integrating the top-down design of PDMS device with the bottom-up design of MT properties. (**A**) Schematic representation of the PDMS device. The device consisted of three areas: MT landing area (between reservoirs C and D), MT sorting area (between reservoirs A and B), and MT alignment area (between MT landing and sorting areas). Channels in the alignment area were 40 μm in length and 5 μm in width. The channel height was 10 μm. (**B**) Image of the fabricated PDMS device. Red ink indicates the channels. Scale bar, 3 mm. (**C**) Bright-field image of the cross section of MT landing, MT alignment, and MT sorting areas. Channels are filled with ink without leakage. Scale bar, 50 μm. (**D**) Sequential images of MT immobilization in the MT landing area. Flow generated by pressure differences among reservoirs prevented MTs from escaping to the MT alignment area. White solid lines represent the wall. Scale bar, 20 μm. Fluorescent images of MTs in (**E**) the MT landing area and (**F**) MT alignment area. Scale bar, 20 μm. Histograms of MT orientation angles in (**G**) MT landing (n = 70) and (**H**) MT alignment areas (n = 35). Probabilities are represented by blue bars. MT gliding directions were aligned in the MT alignment area with significant decreases in the SDs of the orientation angles. Bin width = π/19 rad. (**I**) MT-2 (purple dashed lines) and MT-5 (red solid lines) were sorted with 57.7% efficiency (n = 129). (**J**) MT-2 (purple dashed lines) and MT-5′ (orange solid lines) were sorted with 80.4% efficiency (n = 159). Blue triangles represent the PDMS separation wall. An electric field of 3 kV m^{-1} was applied in the negative x direction. The upper right corners of the MT alignment area are set to origin.

equal to the distance between kinesins; however, our calculated $\langle d \rangle$ values are much larger than the distance between kinesins measured in most previous reports: 0.16 μm measured for the kinesin concentration of 0.2 mg ml^{-1} (*63*), 0.10 μm for 0.07 mg ml^{-1} (*17*), and 0.4 μm for 1.0 μg ml^{-1} (*14*). Only one group reported a larger spacing of about 4 μm using an MT-bound microbead manipulated by optical

tweezers (*64*, *65*). Furthermore, why would the distance between kinesins depend on the MT L_p?

There are three possible explanations why $\langle d \rangle$ calculated from the measured L_p and R_{MT} was larger than the distance between kinesins. The first reason could be due to the flexibility of the stalk region of kinesin. Kinesins bound to the MT tips could be extended until detachment when the electric field was applied to bend the MT. In such a situation, the foremost kinesin is not at the clamped end, and the free tip length, deformed by an electric field, becomes larger than the actual distance between kinesins (*14*). One issue with this possibility is that the kinesin stalk is on the order of tens of nanometers; therefore, it cannot account for the several micrometers measured for $\langle d \rangle$.

A second possible explanation is a change of $\langle d \rangle$ while gliding due to the change of kinesin detachment rate, k_{off}. This was not considered in previously reported distances between kinesins. However, kinesin molecules easily detach from the MTs in the presence of ATP because of the significant increase in k_{off} (0.0009 s^{-1}, without ATP, to 0.66 s^{-1} at 1 mM ATP) (*66*). After introducing the ATP solution to initiate MT gliding, some kinesin molecules at MT leading tips detach because of the increase of k_{off}, resulting in a larger apparent tip length, $\langle d \rangle$.

A third explanation may be due to the deviation of the MT trajectories from the approximation model. The model is derived by assuming that the infinitesimal deformation theory is applicable (*67*). When many kinesins are stretched or detached from leading tips, they experience a large deformation, and the model is no longer applicable at the microscopic level. To justify the approximation model, we estimated the maximum deflection at the free end, y_{max}, by

$$y_{max} = \frac{c_{\perp}\left(\mu_{el} - \mu_{EOF}\right) E \langle d \rangle^4}{8\kappa} \quad (3)$$

The ratio of y_{max} to $\langle d \rangle$ was smaller than 5 to 2.8% for MT-2, 3.3% for MT-5, and 3.8% for MT-5′. The squared $y_{max}/\langle d \rangle$ was up to 0.005, which satisfied the assumption of the infinitesimal deformation theory, that is, the squared $y_{max}/\langle d \rangle$ should be much smaller than 1. Therefore, the approximation model was appropriate, and we can reject the third reason.

By considering these explanations, the calculated $\langle d \rangle$ value differed from the actual distance between kinesins. Therefore, we proposed a strategy to directly measure R_{MT} in a flow cell to define the dimension of a microfluidic device, rather than to calculate R_{MT} by measuring L_p, and the distance between kinesins. Once the $\langle d \rangle$ was calculated from L_p and the measured R_{MT}, one can use the $\langle d \rangle$ for any experimental setup to estimate R_{MT} for the design of a microfluidic device. As long as the cantilever model can be applied and Eq. 2 is effective, our design methodology requires an assay to measure L_p and R_{MT} to derive $\langle d \rangle$, which can be applied to design the molecular sorting device.

In summary, the integration of the bottom-up design of the MT properties, with the top-down design of a microfluidic device, enabled us to create a highly efficient autonomous MT sorting system. Current state-of-the-art assays for MT shuttle sorting require direct imaging and user input for controlling electric fields (*16*). Here, the autonomous nature of sorting due to manipulation of electrical and mechanical properties of the MTs and the optimization of channel design makes this an important advance. For the bottom-up approach, the stiffness of MTs was modified by polymerizing conditions: The growth rate and nucleotide type and the relationship between their persistence length, L_p, and radius of curvature, R_{MT}, were determined. Stiff MTs showed larger R_{MT} than soft MTs as estimated by the cantilever model. Additional electrical modifications to soft MTs further decreased the R_{MT}. For the top-down approach, the structure of the device and field intensity was optimized on the basis of the measured R_{MT}. Thus, the sorting efficiency reached ~60% with L_p-modified MTs and ~80% with both surface charge density– and L_p-modified MTs, which exceeds a previously reported efficiency (~69%) with the active control of electric fields (*16*). The combined top-down and bottom-up design methodology is essential to attain autonomous directional control of molecular shuttles. In conjunction with other molecular shuttle–based techniques, various molecular functions can be integrated into the same microfluidic device: Target analytes can be transported by loading them onto molecular shuttles (*5*–*10*), can be concentrated by capturing the molecular shuttles with chemical reactions (*10*) or collector structures (*5*), and can be detected by conjugating the analytes with fluorescently labeled dye (*8*). Our proposed design methodology overcomes the difficulties in using kinesin-driven MTs as well-controlled molecular shuttles in μTAS. We believe that the biocompatible molecular shuttles can be used as nanorobots with ubiquitous applications in nanobiotechnology.

MATERIALS AND METHODS

Reagent preparation

Reagents were purchased from Sigma-Aldrich unless otherwise stated. Tubulin was purified from porcine brains by two cycles of polymerization and depolymerization followed by a phosphocellulose column, as previously described (*68*). Recycled tubulin was purified from the tubulin by one more cycle of polymerization and depolymerization to remove any nonpolymerized tubulin. Succinimidyl ester–conjugated tetramethylrhodamine (C-1171; Invitrogen) or Alexa Fluor 488 (A-20000; Invitrogen) was labeled by adding 50 or 15 M excess dye to tubulin, respectively (*69*). Human kinesin (amino acid residues 1 to 573) with an N-terminal histidine tag was purified as previously reported (*70*). Purified proteins were stored in liquid nitrogen. DNA molecules were purchased from JBioS. These were hybridized by incubating 5′ biotinylated single-strand DNA (ssDNA) with 5′ Alexa Fluor 488–labeled complementary ssDNA at 1:1 molar ratio at 37°C for >20 min. The sequence was 5′-GAGGTCTTAACGGTGGAGGATGGGGGTTA-GTCCGGGGCGCAGATTCGAAT-3′. We used a BRB80 buffer [80 mM Pipes, 1 mM $MgCl_2$, and 1 mM EGTA (pH 6.8) with KOH] for the dilution and suspension of proteins unless otherwise stated. Tau proteins (2N4R) were purchased from rPeptide.

Measurement of MT growth rate

The growth rate was measured for the elongated segment from a seed MT. Seed MTs were polymerized by incubating recycled tubulin and Alexa Fluor 488–labeled tubulin at 2:1 in the presence of 1 mM dithiothreitol (DTT) (048-29224; Wako) and 1 mM GMPCPP (NU-405S; Jena Bioscience) at 37°C for 30 min. The seeds were stabilized in 20 μM paclitaxel after polymerization and elongated from both ends by incubating with tubulin at a total concentration of 10 or 30 μM, which consisted of nonlabeled, recycled, and tetramethylrhodamine-labeled tubulins at a molar ratio of 1.3:0.4:1, in the presence of 1 mM $MgSO_4$ (131-00405; Wako) and 1 mM GTP at 37°C for 60 min. The final paclitaxel concentration during elongation was 2 μM. MTs were sampled at 0, 0.5, 1, 1.5, 2, 2.5, 3, 4, 5, 7.5, 10, 15, 20, 30, and 60 min after starting the incubation to measure the growth rate. Sampled MTs were diluted to 0.1 μM (below the critical concentration) in the presence of 20 μM paclitaxel and centrifuged

(163,000*g* and 27°C for 20 min) to remove the nonpolymerized tubulin. The precipitated MTs were resuspended and introduced into a flow chamber constructed by two coverslips (C218181 and C024361; Matsunami Glass) and 50-μm-thick double-sided tape (400P50; Kyodo Giken Chemical). After a 5-min incubation for nonspecific binding of MTs to the glass substrate, the chamber was washed out and sealed with clear nail polish. The elongated length of the tetramethylrhodamine-labeled MT segment was measured with FIESTA by fitting the MT shape with the subpixel resolution via Gaussian fitting. Extremely short MTs (<500 nm) (that is, just after the start of elongation) could not be detected by FIESTA. When the number of undetectable MTs exceeded that of the detectable MTs, we did not use the image to measure the MT length. The MT growth rate was defined by fitting initial time data to a linear equation where the slope reports the rate of growth ($R^2 > 0.90$). We used only length distributions that were normally distributed.

Experimental procedures for L_p measurement

MT-1 to MT-5 were extended from Alexa Fluor 488–labeled biotinylated MT seeds. After the preparation of MT seeds as stated in the section above, they were biotinylated by incubating with a 20-fold molar excess of biotin-XX succinimidyl ester (B1606; Invitrogen) to tubulin at 37°C for 30 min. After quenching the unreacted biotin with a 200-fold molar excess of potassium glutamate to tubulin at 37°C for 10 min, they were shortened by shearing through a 30-gauge syringe needle (90030; Osaka Chemical) (*5*). Seeds were stabilized with 20 μM paclitaxel after centrifugation and elongated from both ends at 37°C for >20 min under five different conditions: GMPCPP and 10 μM tubulin with tau (MT-1) and without tau (MT-2), GTP and 10 μM tubulin with tau (MT-3) and without tau (MT-4), and GTP and 30 μM tubulin without tau (MT-5). The tau concentration was 1 μM, 10-fold lower than tubulin. All MTs were stabilized by 20 μM paclitaxel after polymerization.

Glass coverslips were cleaned in acetone, isopropanol, and HNO_3 in order and rinsed in deionized water (DIW). They were dried with nitrogen gas and exposed to air plasma (Covance MP; Femto Science). Then, they were immersed in a mixture of biotin-PEG-silane (1 mg ml^{-1}) (MW3400, Biotin-PEG-SIL-3400-1g; Laysan Bio), 30 mM HCl, and 97% ethanol in a nitrogen chamber overnight. They were rinsed in ethanol and DIW and dried for storage at 4°C until use (*32*).

Flow chambers were constructed by bonding the biotin-coated coverslip to a noncoated coverslip with double-sided tape (10-μm thickness, 7070W; Teraoka Seisakusho). We introduced streptavidin (2 mg ml^{-1}) (192-11644; Wako) and incubated for 3 min. After washing out the chambers with BRB80, the partially biotinylated MTs (MT-1 to MT-5) were immobilized via biotin-streptavidin bindings by a 5-min incubation. Nonimmobilized MTs were removed by flowing through BRB80, which included an O_2 scavenger system [BRB80-O_2; catalase (8.0 μg ml^{-1}), 25 mM D-glucose, glucose oxidase (20 μg ml^{-1}), 1% 2-mercaptoethanol, 20 mM DTT, 3.0 mM 1,1′-ferrocenedimethanol (322-49071; Wako), and 20 μM paclitaxel in BRB80]. Last, the chamber was sealed with clear nail polish to prevent flow.

L_p was measured at room temperature (~27°C). MT shapes were analyzed with a custom-written MATLAB algorithm (MathWorks) as reported previously (*60*). Briefly, we expressed the MT shape as a superposition of Fourier modes and measured MT bending energy from their deformation on the assumption that the elongated segment behaved as a cantilever clamped at an immobilized biotinylated segment. Because MT fluctuations originated only from thermal energy in the sealed chamber, the MT bending energy was equated with thermal energy, which enabled us to derive L_p. The analysis procedure has been published in previous reports (see the Supplementary Materials and fig. S2 for details) (*27*, *34*, *60*).

Fabrication of the PDMS device

A bare silicon wafer was dehydrated at 200°C for 5 min and spin-coated with hexamethylsilazane at 500 revolutions per minute (rpm) for 5 s and 3000 rpm for 40 s to increase the adhesiveness of an SU-8 resist (1H-D7; Mikasa). After baking the hexamethylsilazane at 120°C for 5 min, an SU-8 3010 photoresist (MicroChem) was spin-coated at 500 rpm for 10 s (ramp, 100 rpm s^{-1}) and 3000 rpm for 30 s (ramp, 300 rpm s^{-1}), followed by baking at 65°C for 2 min, 95°C for 3 min, and 65°C for 1 min in that order. The channel pattern drawn on a Cr mask (HS Hardmask Blanks; Clean Surface Technology Co.) was transferred by a mask aligner (PEM-800; Union), with an exposure energy of 200 mJ cm^{-2}, and baked at 65°C for 1 min, 95°C for 2 min, and 65°C for 3 min. The wafer was cooled at room temperature for 5 to 10 min, and SU-8 was developed by immersion in a developer (MicroChem) at 40°C for 3 min. After rinsing with isopropyl alcohol at 40°C for 10 s and drying, the SU-8 mold was silanized overnight in a vacuum chamber filled with gaseous trichloro(1*H*,1*H*,2*H*,2*H*-perfluorooctyl) silane to enable easy peeling of the cured PDMS.

A PDMS prepolymer was mixed with a curing agent (SILPOT 184 W/C; Dow Corning Toray) at a ratio of 10:1 (w/w) and cast onto the SU-8 mold at a thickness of ~5 mm. It was then degassed in a vacuum chamber for 30 min and cured at 80°C for 2 hours. The cured PDMS was peeled from the mold and punched with a biopsy punch (Sterile Dermal Biopsy Punch, 3 mm; Kai Industries) to make reservoirs. Coverslips were cleaned in 10N KOH solutions at room temperature for 24 hours and rinsed twice by ultrasonication in DIW at room temperature for 20 min. They were then immersed in 20% ethanol solution at room temperature for 10 min and rinsed in DIW, followed by drying with nitrogen gas. The PDMS and the cleaned coverslips were exposed to air plasma and bonded permanently.

Experimental procedures for R_{MT} measurement

MT-1, MT-2, and MT-5 without GMPCPP seeds were polymerized for R_{MT} measurement. MT-1 was polymerized under 1 mM GMPCPP and 1 mM tau using 10 μM tubulin. MT-2 was polymerized under 1 mM GMPCPP and 10 μM tubulin without tau. MT-5 was polymerized under 1 mM GTP and 30 μM tubulin without tau. For the preparation of MT-5′, the shortened MT-5 was biotinylated and elongated only from the plus end by incubating it with a mixture of nonfluorophore-labeled, *N*-ethylmaleimide (NEM)–treated, and fluorophore-labeled tubulin in the presence of 1 mM $MgSO_4$ and 1 mM GTP at 37°C for 30 min. NEM-treated tubulin was prepared by incubating the recycled tubulin with 1 mM GTP and 300 to 500 M excess of NEM (10 mM) at 4°C for 10 min, followed by incubation with 0.56% 2-mercaptoethanol at 4°C for 10 min to inactivate the excess NEM (*69*). MT-5 biotinylated at the minus end was centrifuged, resuspended with 20 μM paclitaxel, and labeled with the hybridized DNA at 37°C.

A PDMS channel was coated with Pluronic F108 (2 mg ml^{-1}) (BASF) to prevent kinesin binding onto the PDMS surfaces, and then, kinesin (0.08 mg ml^{-1}) with casein (1.9 mg ml^{-1}) was immobilized. These solutions introduced from reservoir A were incubated for 5 min and washed out with BRB80. Four types of MTs were introduced, all reservoirs were filled with 0.5 mM ATP diluted with BRB80-O_2, and platinum electrodes were inserted into reservoirs A and B. An electric field from reservoir B to reservoir A was applied with an average intensity of 5.3 kV m^{-1} (E3612; Agilent Technologies).

MTs were tracked at the leading tips with Mark2 software (provided by K. Furuta, National Institute of Information and Communications Technology), and their trajectories were fitted by Eq. 1 to obtain R_{MT}. The MTs gliding discontinuously or turning on a pivot were removed from the analysis.

MT sorting

The PDMS channel was coated with Pluronic F108, kinesin, and casein sequentially. To immobilize MTs on the landing area surface only, we introduced 5 μl of BRB80-O_2 to reservoirs A and B, and then, 5 μl of an MT mixture (MT-2 and MT-5, or MT-2 and MT-5′) was loaded into reservoir C, resulting in a flow toward empty reservoir D from the other reservoirs. The MT solution in reservoir C was removed, and the landing area was washed out by 5 μl of BRB80-O_2. An electric field was applied from reservoir B to reservoir A via platinum electrodes inserted into ATP-filled reservoirs. The average field intensity was set to 3.0 kV m^{-1}. MT sorting was visualized with ImageJ software (National Institutes of Health) with the MTrackJ plug-in (*71*). MTs were tracked at the leading tips at 15-s intervals once they entered from MT alignment to the sorting area along the *y* axis.

Optical imaging and analysis

MT and DNA molecules were observed under an IX73 inverted epi-fluorescence microscope (Olympus) with an excitation filter (GFP/DsRed-A-OMF; Opto-Line International Inc.), a complementary metal-oxide-semiconductor camera (ORCA-Flash 4.0 V2; Hamamatsu Photonics), image-splitting optics (W-VIEW GEMINI; Hamamatsu Photonics) with a band-pass emitter (FF01-512/25-25 and FF01-630/92-25; Semrock) and dichroic mirror (FF560-FDi01-25x36; Semrock), and oil-immersion objectives. The magnification, exposure time, frame rate, and recording period were 100× [numerical aperture (NA), 1.4], 100 ms, 2.5 frames per second, and 200 s for observing MT thermal fluctuation and 60× (NA, 1.35), 200 ms, 0.33 to 0.5 frames per second, and >1 hour for observing MT gliding, respectively. An ND6 filter was used with a shutter (VMM-D3; Uniblitz). Optical images were stored as sequential image files in TIFF format using HCImage software (Hamamatsu Photonics).

Multiple significance tests were performed among all data by Steel-Dwass tests at a critical value of $P < 0.01$, and normality or log-normality was tested among outlier-removed data by Lilliefors tests at a critical value of $P > 0.05$. All curve fittings were performed by the least-squares methods of MATLAB.

SUPPLEMENTARY MATERIALS

robotics.sciencemag.org/cgi/content/full/2/10/eaan4882/DC1
Supplementary Text
Fig. S1. Histogram of MT length at each sampling time.
Fig. S2. Details for measuring L_p of MTs.
Fig. S3. Histograms of L_p for MT-1 to MT-5.
Fig. S4. Scatterplots of L_p versus length for MT-1 to MT-5.
Fig. S5. Histograms of R_{MT} for MT-1, MT-2, MT-5, and MT-5′.
Fig. S6. Scatterplots of R_{MT} versus length for MT-1, MT-2, MT-5, and MT-5′.
Fig. S7. Design of the separation wall.
Table S1. Parameter nomenclature.
Movie S1. An example of fluctuating MT-5.
Movie S2. Sorting of MT-2 and MT-5.
Movie S3. Sorting of MT-2 and MT-5′.

REFERENCES AND NOTES

1. K. J. Verhey, J. W. Hammond, Traffic control: Regulation of kinesin motors. *Nat. Rev. Mol. Cell Biol.* **10**, 765–777 (2009).
2. M. J. Schnitzer, S. M. Block, Kinesin hydrolyses one ATP per 8-nm step. *Nature* **388**, 386–390 (1997).
3. R. D. Vale, B. J. Schnapp, T. S. Reese, M. P. Sheetz, Organelle, bead, and microtubule translocations promoted by soluble factors from the squid giant axon. *Cell* **40**, 559–569 (1985).
4. A. Agarwal, H. Hess, Biomolecular motors at the intersection of nanotechnology and polymer science. *Prog. Polym. Sci.* **35**, 252–277 (2010).
5. C.-T. Lin, M.-T. Kao, K. Kurabayashi, E. Meyhofer, Self-contained, biomolecular motor-driven protein sorting and concentrating in an ultrasensitive microfluidic chip. *Nano Lett.* **8**, 1041–1046 (2008).
6. D. Steuerwald, S. M. Früh, R. Griss, R. D. Lovchik, V. Vogel, Nanoshuttles propelled by motor proteins sequentially assemble molecular cargo in a microfluidic device. *Lab Chip* **14**, 3729–3738 (2014).
7. S. Ramachandran, K.-H. Ernst, G. D. Bachand, V. Vogel, H. Hess, Selective loading of kinesin-powered molecular shuttles with protein cargo and its application to biosensing. *Small* **2**, 330–334 (2006).
8. T. Fischer, A. Agarwal, H. Hess, A smart dust biosensor powered by kinesin motors. *Nat. Nanotechnol.* **4**, 162–166 (2009).
9. S. Taira, Y.-Z. Du, Y. Hiratsuka, K. Konishi, T. Kubo, T. Q. P. Uyeda, N. Yumoto, M. Kodaka, Selective detection and transport of fully matched DNA by DNA-loaded microtubule and kinesin motor protein. *Biotechnol. Bioeng.* **95**, 533–538 (2006).
10. S. Hiyama, Y. Moritani, R. Gojo, S. Takeuchi, K. Sutoh, Biomolecular-motor-based autonomous delivery of lipid vesicles as nano- or microscale reactors on a chip. *Lab Chip* **10**, 2741–2748 (2010).
11. Y. Hiratsuka, T. Tada, K. Oiwa, T. Kanayama, T. Q. P. Uyeda, Controlling the direction of kinesin-driven microtubule movements along microlithographic tracks. *Biophys. J.* **81**, 1555–1561 (2001).
12. J. Clemmens, H. Hess, J. Howard, V. Vogel, Analysis of microtubule guidance in open microfabricated channels coated with the motor protein kinesin. *Langmuir* **19**, 1738–1744 (2003).
13. T. Kim, E. Meyhofer, E. F. Hasselbrink, Biomolecular motor-driven microtubule translocation in the presence of shear flow: Modeling microtubule deflection due to shear. *Biomed. Microdevices* **9**, 501–511 (2007).
14. R. R. Agayan, R. Tucker, T. Nitta, F. Ruhnow, W. J. Walter, S. Diez, H. Hess, Optimization of isopolar microtubule arrays. *Langmuir* **29**, 2265–2272 (2013).
15. B. M. Hutchins, M. Platt, W. O. Hancock, M. E. Williams, Directing transport of $CoFe_2O_4$-functionalized microtubules with magnetic fields. *Small* **3**, 126–131 (2007).
16. M. G. L. van den Heuvel, M. P. de Graaff, C. Dekker, Molecular sorting by electrical steering of microtubules in kinesin-coated channels. *Science* **312**, 910–914 (2006).
17. M. G. L. van den Heuvel, M. P. de Graaff, C. Dekker, Microtubule curvatures under perpendicular electric forces reveal a low persistence length. *Proc. Natl. Acad. Sci. U.S.A.* **105**, 7941–7946 (2008).
18. T. Kim, M.-T. Kao, E. F. Hasselbrink, E. Meyhöfer, Active alignment of microtubules with electric fields. *Nano Lett.* **7**, 211–217 (2007).
19. N. Isozaki, S. Ando, T. Nakahara, H. Shintaku, H. Kotera, E. Meyhöfer, R. Yokokawa, Control of microtubule trajectory within an electric field by altering surface charge density. *Sci. Rep.* **5**, 7669 (2015).
20. L. Cassimeris, D. Gard, P. T. Tran, H. P. Erickson, XMAP215 is a long thin molecule that does not increase microtubule stiffness. *J. Cell Sci.* **114** (Pt. 16), 3025–3033 (2001).
21. T. Hawkins, M. Mirigian, M. Selcuk Yasar, J. L. Ross, Mechanics of microtubules. *J. Biomech.* **43**, 23–30 (2010).
22. J. Mizushima-Sugano, T. Maeda, T. Miki-Noumura, Flexural rigidity of singlet microtubules estimated from statistical analysis of their contour lengths and end-to-end distances. *Biochim. Biophys. Acta Gen. Subj.* **755**, 257–262 (1983).
23. R. B. Dye, S. P. Fink, R. C. Williams Jr., Taxol-induced flexibility of microtubules and its reversal by MAP-2 and tau. *J. Biol. Chem.* **268**, 6847–6850 (1993).
24. B. Mickey, J. Howard, Rigidity of microtubules is increased by stabilizing agents. *J. Cell Biol.* **130**, 909–917 (1995).
25. H. Felgner, R. Frank, J. Biernat, E.-M. Mandelkow, E. Mandelkow, B. Ludin, A. Matus, M. Schliwa, Domains of neuronal microtubule-associated proteins and flexural rigidity of microtubules. *J. Cell Biol.* **138**, 1067–1075 (1997).
26. A. Kis, S. Kasas, B. Babić, A. J. Kulik, W. Benoît, G. A. D. Briggs, C. Schönenberger, S. Catsicas, L. Forró, Nanomechanics of microtubules. *Phys. Rev. Lett.* **89**, 248101 (2002).
27. M. E. Janson, M. Dogterom, A bending mode analysis for growing microtubules: Evidence for a velocity-dependent rigidity. *Biophys. J.* **87**, 2723–2736 (2004).
28. C. P. Brangwynne, G. H. Koenderink, E. Barry, Z. Dogic, F. C. MacKintosh, D. A. Weitz, Bending dynamics of fluctuating biopolymers probed by automated high-resolution filament tracking. *Biophys. J.* **93**, 346–359 (2007).
29. J. van Mameren, K. C. Vermeulen, F. Gittes, C. F. Schmidt, Leveraging single protein polymers to measure flexural rigidity. *J. Phys. Chem. B* **113**, 3837–3844 (2009).
30. K. Kawaguchi, A. Yamaguchi, Temperature dependence rigidity of non-taxol stabilized single microtubules. *Biochem. Biophys. Res. Commun.* **402**, 66–69 (2010).

31. T. L. Hawkins, D. Sept, B. Mogessie, A. Straube, J. L. Ross, Mechanical properties of doubly stabilized microtubule filaments. *Biophys. J.* **104**, 1517–1528 (2013).
32. D. Portran, M. Zoccoler, J. Gaillard, V. Stoppin-Mellet, E. Neumann, I. Arnal, J. L. Martiel, M. Vantard, MAP65/Ase1 promote microtubule flexibility. *Mol. Biol. Cell* **24**, 1964–1973 (2013).
33. N. F. Bouxsein, G. D. Bachand, Single filament behavior of microtubules in the presence of added divalent counterions. *Biomacromolecules* **15**, 3696–3705 (2014).
34. F. Gittes, B. Mickey, J. Nettleton, J. Howard, Flexural rigidity of microtubules and actin filaments measured from thermal fluctuations in shape. *J. Cell Biol.* **120**, 923–934 (1993).
35. M. Kikumoto, M. Kurachi, V. Tosa, H. Tashiro, Flexural rigidity of individual microtubules measured by a buckling force with optical traps. *Biophys. J.* **90**, 1687–1696 (2006).
36. F. Pampaloni, G. Lattanzi, A. Jonáš, T. Surrey, E. Frey, E.-L. Florin, Thermal fluctuations of grafted microtubules provide evidence of a length-dependent persistence length. *Proc. Natl. Acad. Sci. U.S.A.* **103**, 10248–10253 (2006).
37. M. Kurachi, M. Hoshi, H. Tashiro, Buckling of a single microtubule by optical trapping forces: Direct measurement of microtubule rigidity. *Cell Motil. Cytoskeleton* **30**, 221–228 (1995).
38. K. M. Taute, F. Pampaloni, E. Frey, E.-L. Florin, Microtubule dynamics depart from the wormlike chain model. *Phys. Rev. Lett.* **100**, 028102 (2008).
39. T. Mitchison, M. Kirschner, Dynamic instability of microtubule growth. *Nature* **312**, 237–242 (1984).
40. M. Zanic, P. O. Widlund, A. A. Hyman, J. Howard, Synergy between XMAP215 and EB1 increases microtubule growth rates to physiological levels. *Nat. Cell Biol.* **15**, 688–693 (2013).
41. J. W. J. Kerssemakers, E. L. Munteanu, L. Laan, T. L. Noetzel, M. E. Janson, M. Dogterom, Assembly dynamics of microtubules at molecular resolution. *Nature* **442**, 709–712 (2006).
42. M. Dogterom, B. Yurke, Measurement of the force-velocity relation for growing microtubules. *Science* **278**, 856–860 (1997).
43. K. Kinoshita, I. Arnal, A. Desai, D. N. Drechsel, A. A. Hyman, Reconstitution of physiological microtubule dynamics using purified components. *Science* **294**, 1340–1343 (2001).
44. R. J. Vasquez, B. Howell, A. M. Yvon, P. Wadsworth, L. Cassimeris, Nanomolar concentrations of nocodazole alter microtubule dynamic instability in vivo and in vitro. *Mol. Biol. Cell* **8**, 973–985 (1997).
45. Y. Komarova, C. O. De Groot, I. Grigoriev, S. M. Gouveia, E. L. Munteanu, J. M. Schober, S. Honnappa, R. M. Buey, C. C. Hoogenraad, M. Dogterom, G. G. Borisy, M. O. Steinmetz, A. Akhmanova, Mammalian end binding proteins control persistent microtubule growth. *J. Cell Biol.* **184**, 691–706 (2009).
46. F. Ruhnow, D. Zwicker, S. Diez, Tracking single particles and elongated filaments with nanometer precision. *Biophys. J.* **100**, 2820–2828 (2011).
47. T. Korten, S. Diez, Setting up roadblocks for kinesin-1: Mechanism for the selective speed control of cargo carrying microtubules. *Lab Chip* **8**, 1441–1447 (2008).
48. B. I. Morshed, M. Shams, T. Mussivand, Analysis of electric fields inside microchannels and single cell electrical lysis with a microfluidic device. *Micromachines* **4**, 243–256 (2013).
49. M. E. Janson, M. Dogterom, Scaling of microtubule force-velocity curves obtained at different tubulin concentrations. *Phys. Rev. Lett.* **92**, 248101 (2004).
50. L. Schaedel, K. John, J. Gaillard, M. V. Nachury, L. Blanchoin, M. Théry, Microtubules self-repair in response to mechanical stress. *Nat. Mater.* **14**, 1156–1163 (2015).
51. S. Wada, A. M. R. Kabir, M. Ito, D. Inoue, K. Sada, A. Kakugo, Effect of length and rigidity of microtubules on the size of ring-shaped assemblies obtained through active self-organization. *Soft Matter* **11**, 1151–1157 (2015).
52. R. D. Vale, C. M. Coppin, F. Malik, F. J. Kull, R. A. Milligan, Tubulin GTP hydrolysis influences the structure, mechanical properties, and kinesin-driven transport of microtubules. *J. Biol. Chem.* **269**, 23769–23775 (1994).
53. B. J. Lopez, M. T. Valentine, Mechanical effects of EB1 on microtubules depend on GTP hydrolysis state and presence of paclitaxel. *Cytoskeleton* **71**, 530–541 (2014).
54. H. Yajima, T. Ogura, R. Nitta, Y. Okada, C. Sato, N. Hirokawa, Conformational changes in tubulin in GMPCPP and GDP-taxol microtubules observed by cryoelectron microscopy. *J. Cell Biol.* **198**, 315–322 (2012).
55. T. Müller-Reichert, D. Chrétien, F. Severin, A. A. Hyman, Structural changes at microtubule ends accompanying GTP hydrolysis: Information from a slowly hydrolyzable analogue of GTP, guanylyl (α,β)methylenediphosphonate. *Proc. Natl. Acad. Sci. U.S.A.* **95**, 3661–3666 (1998).
56. C. Elie-Caille, F. Severin, J. Helenius, J. Howard, D. J. Muller, A. A. Hyman, Straight GDP-tubulin protofilaments form in the presence of taxol. *Curr. Biol.* **17**, 1765–1770 (2007).
57. H. Kadavath, R. V. Hofele, J. Biernat, S. Kumar, K. Tepper, H. Urlaub, E. Mandelkow, M. Zweckstetter, Tau stabilizes microtubules by binding at the interface between tubulin heterodimers. *Proc. Natl. Acad. Sci. U.S.A.* **112**, 7501–7506 (2015).
58. S. Kasas, A. Kis, B. M. Riederer, L. Forró, G. Dietler, S. Catsicas, Mechanical properties of microtubules explored using the finite elements method. *Chemphyschem* **5**, 252–257 (2004).
59. H. Felgner, R. Frank, M. Schliwa, Flexural rigidity of microtubules measured with the use of optical tweezers. *J. Cell Sci.* **109** (Pt. 2), 509–516 (1996).
60. T. L. Hawkins, M. Mirigian, J. Li, M. S. Yasar, D. L. Sackett, D. Sept, J. L. Ross, Perturbations in microtubule mechanics from tubulin preparation. *Cell. Mol. Bioeng.* **5**, 227–238 (2012).
61. P. Venier, A. C. Maggs, M.-F. Carlier, D. Pantaloni, Analysis of microtubule rigidity using hydrodynamic flow and thermal fluctuations. *J. Biol. Chem.* **269**, 13353–13360 (1994).
62. J. Zhang, C. Wang, Molecular structural mechanics model for the mechanical properties of microtubules. *Biomech. Model. Mechanobiol.* **13**, 1175–1184 (2014).
63. J. Ikuta, N. K. Kamisetty, H. Shintaku, H. Kotera, T. Kon, R. Yokokawa, Tug-of-war of microtubule filaments at the boundary of a kinesin- and dynein-patterned surface. *Sci. Rep.* **4**, 5281 (2014).
64. T. L. Fallesen, J. C. Macosko, G. Holzwarth, Force–velocity relationship for multiple kinesin motors pulling a magnetic bead. *Eur. Biophys. J.* **40**, 1071–1079 (2011).
65. T. L. Fallesen, J. C. Macosko, G. Holzwarth, Measuring the number and spacing of molecular motors propelling a gliding microtubule. *Phys. Rev. E Stat. Nonlin. Soft Matter Phys.* **83**, 011918 (2011).
66. W. O. Hancock, J. Howard, Kinesin's processivity results from mechanical and chemical coordination between the ATP hydrolysis cycles of the two motor domains. *Proc. Natl. Acad. Sci. U.S.A.* **96**, 13147–13152 (1999).
67. S. P. Timoshenko, *Strength of Materials: Elementary Theory and Problems* (Van Nostrand Reinhold, ed. 3, 1958), vol. 1, pp. 359.
68. R. C. Williams Jr., J. C. Lee, Preparation of tubulin from brain. *Methods Enzymol.* **85** (Pt. B), 376–385 (1982).
69. A. Hyman, D. Drechsel, D. Kellogg, S. Salser, K. Sawin, P. Steffen, L. Wordeman, T. Mitchison, Preparation of modified tubulins. *Methods Enzymol.* **196**, 478–485 (1991).
70. R. Yokokawa, M. C. Tarhan, T. Kon, H. Fujita, Simultaneous and bidirectional transport of kinesin-coated microspheres and dynein-coated microspheres on polarity-oriented microtubules. *Biotechnol. Bioeng.* **101**, 1–8 (2008).
71. E. Meijering, O. Dzyubachyk, I. Smal, Methods for cell and particle tracking, in *Methods in Enzymology*, P. M. Conn, Ed. (Academic Press, 2012), vol. 504, chap. 9, pp. 183–200.

Acknowledgments: We thank K. Furuta for the software, Mark2, for tracking the MT trajectories. **Funding:** This study was partially supported by Precursory Research for Embryonic Science and Technology from the Japan Science and Technology Agency; Japan Society for the Promotion of Science (JSPS) KAKENHI (grant numbers 25709018 and 17H03206); Kyoto University Supporting Program for Interaction-Based Initiative Team Studies as part of the Program for Promoting the Enhancement of Research Universities, the Ministry of Education, Culture, Sports, Science and Technology (MEXT), Japan; Kyoto University NanoTechnology Hub in "Nanotechnology Platform Project" sponsored by MEXT, Japan. N.I. was supported by Grant-in-Aid for JSPS Research Fellow (grant number 262439). J.L.R. was supported by a grant from the Mathers Foundation, Moore Foundation (grant 4308.1), NSF INSPIRE (award MCB-1344203), and the Department of Defense Army Research Office Multidisciplinary University Research Initiative (MURI; 67455-CH-MUR MURI award). T.L.H. was supported by the Wisconsin Space Grant and University of Wisconsin–La Crosse Faculty Research Grant. **Author contributions:** N.I. and R.Y. designed the experiments. N.I. performed the experiments and analyzed the data. All authors discussed and interpreted the results, and N.I., T.L.H., J.L.R., and R.Y. wrote the paper. All authors have given approval to the final version of the manuscript. **Competing interests:** The authors declare that they have no competing financial interests. **Data and materials availability:** All data for the conclusion in the paper are present in the paper and/or the Supplementary Materials. Contact R.Y. for additional information including source code.

Submitted 29 May 2017
Accepted 6 September 2017
Published 27 September 2017
10.1126/scirobotics.aan4882

Citation: N. Isozaki, H. Shintaku, H. Kotera, T. L. Hawkins, J. L. Ross, R. Yokokawa, Control of molecular shuttles by designing electrical and mechanical properties of microtubules. *Sci. Robot.* **2**, eaan4882 (2017).

Science Robotics

Control of molecular shuttles by designing electrical and mechanical properties of microtubules

Naoto Isozaki, Hirofumi Shintaku, Hidetoshi Kotera, Taviare L. Hawkins, Jennifer L. Ross, and Ryuji Yokokawa

Sci. Robot. **2** (10), eaan4882. DOI: 10.1126/scirobotics.aan4882

Science Robotics (ISSN 2470-9476) is published by the American Association for the Advancement of Science. 1200 New York Avenue NW, Washington, DC 20005. The title *Science Robotics* is a registered trademark of AAAS.